Title
Design of a Dexterous Three-Fingered Hand Exoskeleton for Stroke Patient Rehabilitation

Author
Dimapasoc, Brando

Publication Date
2017

Peer reviewed|Thesis/dissertation

UNIVERSITY OF CALIFORNIA

Los Angeles

Design of a Dexterous Three-Fingered Hand Exoskeleton for Stroke Patient Rehabilitation

A thesis submitted in partial satisfaction

of the requirements for the degree Master of Science

in Mechanical Engineering

by

Brando Dimapasoc

2017

ABSTRACT OF THE THESIS

Design of a Dexterous Three-Fingered Hand Exoskeleton

for Stroke Patient Rehabilitation

by

Brando Dimapasoc

Master of Science in Mechanical Engineering

University of California, Los Angeles, 2017

Professor Jacob Rosen, Chair

Stroke is a leading cause of disability worldwide, and much attention has been focused to technologies to aid in recovery. This thesis details the design of a dexterous hand exoskeleton for use in stroke patient rehabilitation exercises. This device is able to accommodate a wide range of users and can be adjusted to support a number of different grasping motions. The features that allow this versatility are explained. The exoskeleton is actuated through a Bowden cable system and employs an admittance control strategy. The kinematics-based optimization created to design the manipulator links is presented in detail.

The thesis of Brando Dimapasoc is approved.

Veronica Santos

Dennis W. Hong

Jacob Rosen, Committee Chair

University of California, Los Angeles

2017

Table of Contents

List of Figures

List of Tables

CHAPTER 1

Introduction

1.1 Problem Overview

Stroke is a leading cause of disability in adults, with approximately 795,000 people experiencing a new or recurrent stroke annually in the United States [1]. In the aftermath of a stroke up to 80% of victims are initially affected by hemiparesis, or the weakened movement of the contralateral limbs [2]. Another possible effect is spasticity, the damage of communication between the brain and muscles, resulting in tight muscle cramps or spasms, which reduces coordination and muscle movement. Depending on the study and the scale(s) used, it has been found that about 28% of hemiparetic patients were spastic three months after stroke [3]. Another study found that spasticity had a prevalence of 38% in patients studied twelve months after stroke [4]. This impaired movement and dexterity in an upper limb and hand greatly affect the ability of a patient to perform activities of daily living. However, it is believed that the brain exhibits plasticity and can reorganize and adapt to the damage caused by a stroke [5]. With this, the goal of repeated movement in physical therapy following a stroke is to allow the brain to relearn the motor functions it has lost.

1.2 Hand Exoskeletons in Stroke Rehabilitation

A hand exoskeleton is an assistive device worn by a stroke patient to assist in therapeutic exercises during rehabilitation. The device can aid in, guide, and/or react in specific ways to the patient's motions in order to facilitate physical therapy exercises, the goal of which are to allow the patient to relearn the lost motor function in the hemiparetic limb. These devices can also be used to take quantitative data measurements to help characterize and guide a patient's recovery.

Hand exoskeletons have taken on many forms and use different mechanisms to help the user perform different types of motions and grasps. The human hand has four fingers, each with four degrees of freedom consisting of the rotations of the MCP, PIP, and DIP joints in addition to adduction/abduction. The thumb has five degrees of freedom—three rotations and adduction/abduction as with the fingers, and also opposition/apposition. Hand exoskeletons have been designed to aid in and train various motions of the hand. Some devices have been created to aid in the binary opening and closing of the hand [6], [7], such as HEXORR shown in Figure 1.1.

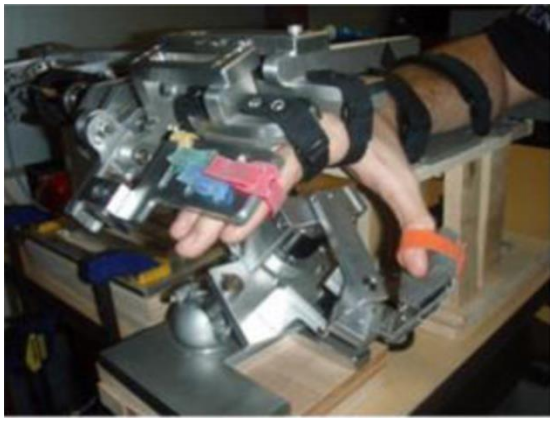

Figure 1.1: HEXORR device for opening and closing of the hand [7].

It is worth noting that in general the interface between the hand and the device depends on the motion(s) that the exoskeleton supports. In the case of the HEXORR, a mitt-esque interface is sufficient to assist in the opening and closing of the hand. Devices that facilitate finer motions of the fingers, such as the flexion and extension of the fingers or pinching [8]–[11], require interfaces that are better tailored for these purposes. These interfaces are usually segmented, such as with the "Hand Exoskeleton (HX)" shown in Figure 1.2. Devices that operate very closely to the user often incorporate features such as passive prismatic joints and adjustable link lengths in order to accommodate the variation in finger sizes among patients.

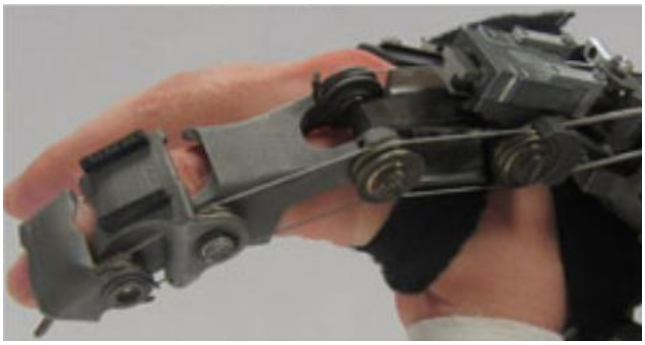

Figure 1.2: HX device with segmented finger interfaces [12].

In terms of actuation, some systems leave one or several degrees of freedom of the hand passive, while many others are actively actuated by motors. Passive devices often use interchangeable or adjustable springs or cords to tune the resistances of certain training motions to the user [6]. For example the BiomHED device [13] shown in Figure 1.3 uses an "exotendon" layout of springs whose overall tension is adjusted by a servo motor.

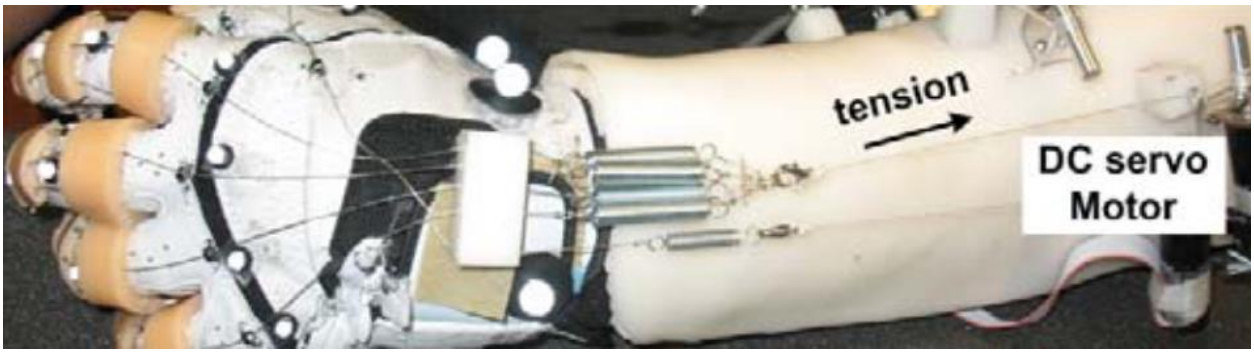

Figure 1.3: BiomHED device with exotendon-style passive actuators [13].

There are several styles of active actuation. One style of active actuation implements a tendon-like system to aid in flexion and extension of the entire hand in an agonist-antagonist manner [14]. Others, such the Actuated Finger Exoskeleton AFX device [9] shown in Figure 1.4 incorporate systems of cables and pulleys [10]. The AFX also includes links that are geared and can move past one another. However, this is not typical, with most designs implementing linkages with fixed attachment points. Some cable-driven systems such as the one shown in Figure 1.5 use Bowden cables to remotely actuate the device [15], [16]. The advantage of such a system is that the distance between the actuator pack and the device itself can be increased. This prevents the patient from having to bear the weight of the actuators while wearing the exoskeleton. It can also remove the need for a tensioning mechanism between the joints of the fingers, which move relative to one another.

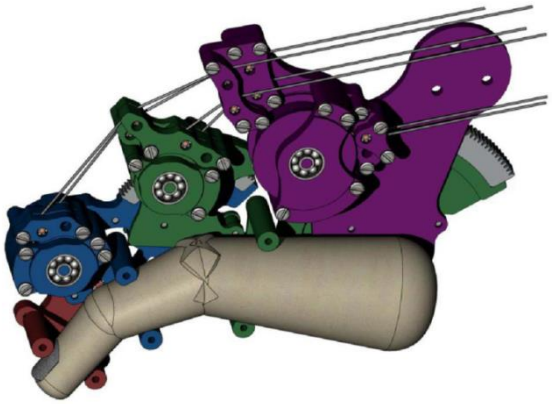

Figure 1.4: AFX device with geared cable transmission actuation [9].

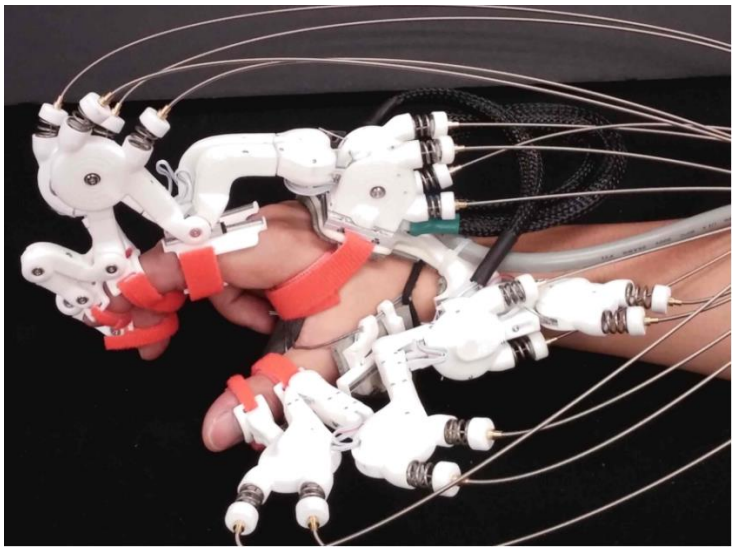

Figure 1.5: Hand exoskeleton with Bowden cable actuation [15].

Another option for actuation includes a motor directly driving a linkage, such as with the four-bar linkage of the IntelliARM [17] shown in Figure 1.6.

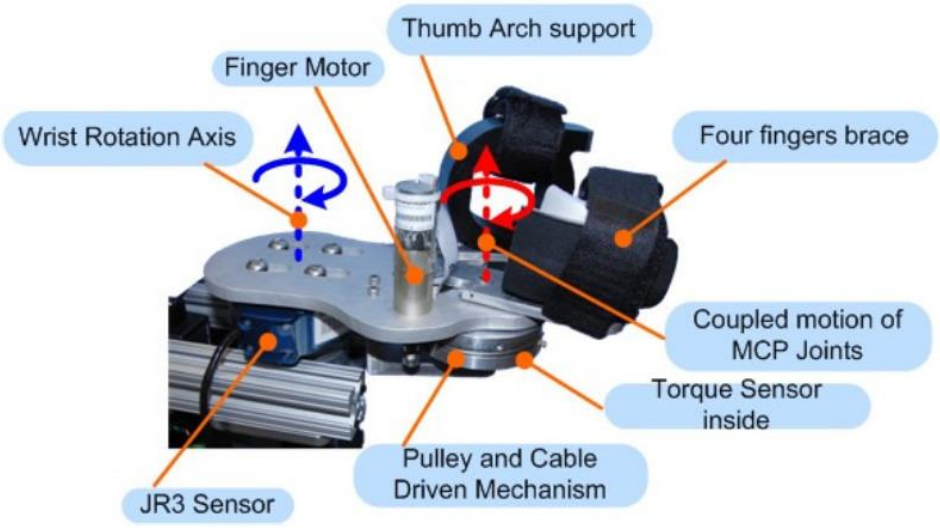

Figure 1.6: IntelliARM hand device [17].

Finally, a number of soft robotic systems involving soft actuation systems have been emerging in recent years as well [18], [19]. Systems such as the one shown in Figure 1.7 include chambers that are actuated via pressurized fluid.

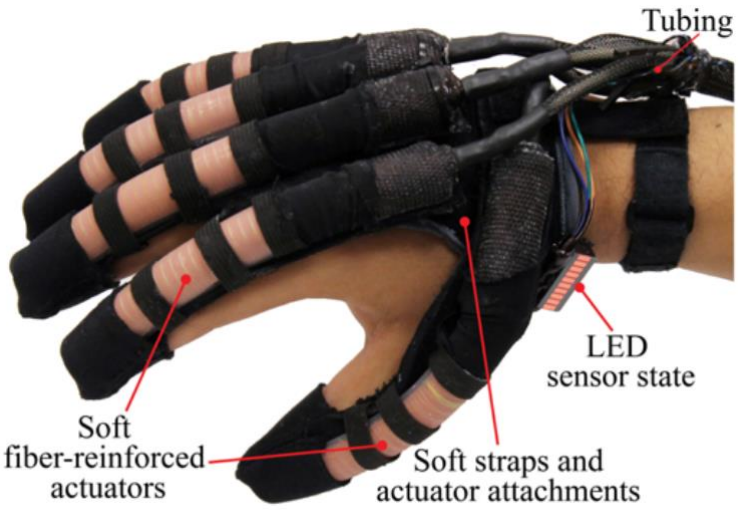

Figure 1.7: Fluid-actuated soft robotic hand exoskeleton [18].

Common ways to control these exoskeletons include admittance and impedance control, as well as sEMG [19]–[21].

Table 1.1 provides a summary of relevant past research in hand exoskeleton devices. As evidenced by the variety of devices that have been produced in the past, creating an assistive or rehabilitative exoskeleton for the hand is a complex problem with many factors that must be taken into account and addressed by the design.

Table 1.1: Summary of Relevant Devices

Device	# Degrees of Freedom	Sensing for Control System	Actuation System	Additional Features/Notes
HandSOME [6]	1 (passive)	Force/Torque Sensor	Cords/springs	Supports pinch-pad grasp. Passively-actuated.
HEXORR [7]	1 (active)	Torque sensor	Electric motor with four-bar linkage	Supports opening and closing of the hand.
Y. Fu and S. Wang [8]	4 per finger (active)	Force sensor	Electric motors with gear system and flexible cables	Supports finger flexion/extension and adduction/abduction.
Actuated Finger Exoskeleton (AFX) [9]	3 (active)	Cable tension sensors	Antagonistic cables and motor system	Supports one finger in a pinching motion.
Cable Actuated Finger Exoskeleton (CAFE) [10]	3 (active)	Force sensors at finger segments	Electric motors and cables	Supports one finger. Actuators mounted on plate.
P. Agarwal et al. [11], [15]	4 for finger (2 active, 2 passive)	Torque sensors	Electric Motors with Bowden Cable Transmission	Uses series elastic actuation and prismatic passive joint over proximal phalanx.
Hand Exoskeleton (HX) [12]	Finger: 7 (3 passive, 4 active) Thumb: 9 (6 passive, 3 active)	To-be-implemented. Currently position sensors.	Electric motors with Bowden cable transmission	Features self-alignment mechanisms.
BiomHED [13]	Finger: 4 supported (passive) Thumb: 5 supported (passive)	None	Electric motor with spring and exotendon cable system	Servo motor sets cable tensions to provide resistance for various hand motions.
HANDEXOS [14]	4 per finger (2 active, 2 passive)	Force sensors	Motor with gear and antagonistic Bowden cable System	Passive prismatic DOF along proximal phalanx segment.
READAPT [16]	2 per finger (active) 4 for thumb (active)	Joint torques sensed using series elastic actuators	Electric motor and Bowden cable transmission	Integrated hand and wrist exoskeleton.
IntelliARM [17]	1 for hand	Torque sensor	Electric motor with four-bar linkage	Supports opening and closing of the hand as part of an arm exoskeleton.
P. Polygerinos et al. [18]	3 per finger 2 for thumb	Multi-axis force/torque sensors	Soft actuators with tubing and pressured fluid	Soft actuators curl in segments unlike traditional linkages
A Helping Hand [19]	3 supported for fingers	EMG signals (armband) and Optical fiber strain sensors	Elastomeric vessels with pressurized fluid	Soft actuators and orthosis body.

1.3 Outline

The following chapters present the design of an actively-actuated three-fingered dexterous hand exoskeleton for use in stroke patient rehabilitation. The requirements for and mechanical design of the device are described and discussed in Chapter 2. The form of the exoskeleton and the actuation system are presented in detail. Chapter 3 focuses on the kinematics-based optimization method used to design the manipulators of the exoskeleton. In Chapter 4, the strategy behind the control system is presented.

CHAPTER 2

Exoskeleton Design

2.1 Outline

In this chapter, the exoskeleton design is presented. First, the general requirements for the design are listed. Following this is a description of various aspects of the design including the manipulator kinematics, interfaces with the patient, and actuation system. The rationale behind these design choices and how they fulfill the aforementioned design requirements are discussed.

2.2 The Exoskeleton

A CAD rendering of the final design of the hand exoskeleton is shown in Figure 2.1 below.

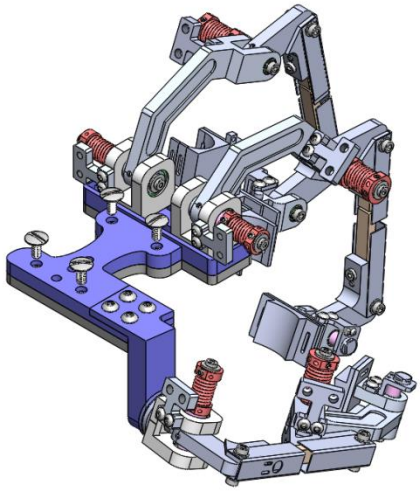

Figure 2.1: The Final Design of the Hand Exoskeleton.

2.3 Design Considerations

The general requirements for the device listed below were set prior to the start of the design process.

1. The device must be able to accommodate a wide range of hands, including at least the 95th percentile hand size.
2. The manipulators must allow the user to practice and perform a number of different grasp types and hand motions, as opposed to just a binary opening and closing of the hand.
3. The device must have a way for both the hand itself and the actuators to be integrated into the existing EXO-UL7 upper-limb exoskeleton.
4. To keep the hand itself lightweight, the actuators must be able to control the system remotely.

2.4 General Form of the Exoskeleton

The exoskeleton hand is comprised of three serial 3R planar mechanisms. This decision was made to allow the manipulator to have the flexibility required to reach the entire areas of the digits' in-plane workspaces without interfering with the digit itself. The choice to use the three manipulators stems from 95% of human grasps being achievable with three digits—a thumb and two fingers—and the human hand is redundant in having five digits [22].

Two of these mechanisms are based on the dorsal side of the hand above the fingers' MCP joints. The third is based on the dorsal side of the thumb above the CMC joint and controls the thumb. All manipulators control the digits from their dorsal sides to prevent interference at the sides of the digits and to allow the user to grasp objects while using the exoskeleton. Each manipulator's end effector interfaces with the digit tip and operates in the plane of the digit. The two finger linkages can control the fingers in different groupings. One of the finger linkages will always be controlling the index finger no matter the finger combination, and the other will always be controlling the little finger. Figure 2.2 shows a kinematic diagram for how the manipulator controls a single finger. The same principal applies to the thumb manipulator, but with the CMC joint replacing the MCP joint. Each of the revolute joints shown rotates about an axis pointing out of the page.

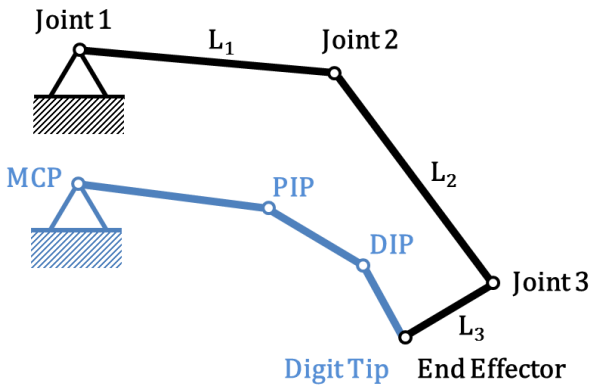

Figure 2.2: Kinematic diagram of the manipulator (black) and finger(s) (blue) modeled as 3R planar mechanisms.

The link lengths of each of the three manipulators are recorded below in Table 2.1. These link lengths were obtained via an optimization method that is detailed in Chapter 3. The lengths used for the digits' bones were those of the 95th percentile based on a hand anthropometry study of U.S. Army Personnel. These values are shown in Table 2.2.

Table 2.1: Link Lengths of the Exoskeleton Manipulators

	Index Finger Manipulator	**Little Finger Manipulator**	**Thumb Manipulator**
L_1	3.0 in	3.0 in	2.96 in
L_2	3.5 in	3.5 in	2.08 in
L_3	1.75 in	1.6 in	2.09 in

Table 2.2: Digit Bone Lengths of the 95th Percentile [23]

	Index Finger	**Little Finger**		**Thumb**
Proximal Phalanx	2.79 in	1.87 in	**Thumb Metacarpal**	3.72 in
Medial Phalanx	1.06 in	0.83 in	**Proximal Phalanx**	1.03 in
Distal Phalanx	1.27 in	1.23 in	**Distal Phalanx**	1.53 in

2.5 Degrees of Freedom

Given that each manipulator has three joints, the decision must be made as to which joints are active, and which—if any—are passive. For this device, Joints 1 and 2 of each 3R planar manipulator are actively actuated, while Joint 3 remains passive. The reasoning for this decision is as follows:

The device must be able to control the position of the digit within its workspace. Actuating only one joint would give the least amount of control over the digit position. Therefore, more than one joint must be actuated. One option is to actively actuate all three joints. This would provide the greatest control over the position of the end effector and the digit tip. However, user comfort would entail controlling the third joint in such a way that the digit tip's orientation is comfortable to the user. This is a difficult task because different users will have digits of varying sizes, and predicting what third joint angles and end effector orientations are comfortable to the user in different areas of the workspace would be challenging and necessary. In addition, this option requires the greatest number of motors overall for the hand, which makes both the hand exoskeleton and the actuator pack larger and heavier. Therefore, the decision was made to not actively actuate all three joints.

The remaining option is to choose two joints to actuate. Through optimization, which will be discussed in detail in a following chapter, it was found that the third link is the shortest in length for each manipulator. This implies that the angle of the third joint has the least influence on the position of the end effector and caters mostly towards the orientation of the end effector. It follows that actuating the first two joints, which correspond to the first and second links, affords the most control over the position of the end effector. Leaving the third joint passive then allows the user's digits to naturally orient themselves in a way that the user finds comfortable.

Others motions of the fingers to address are adduction and abduction. These motions are not actively actuated in the interest of reducing the device's overall size and weight. However, not accommodating adduction and abduction at all restricts the natural motions of the fingers and makes movement stiff and entirely in-plane. Therefore, adduction and abduction are passively allowed over small angle ranges via a rotational axis on the third link of each finger manipulator. Figure 2.3 shows a kinematic schematic of the degrees of freedom of the finger manipulators.

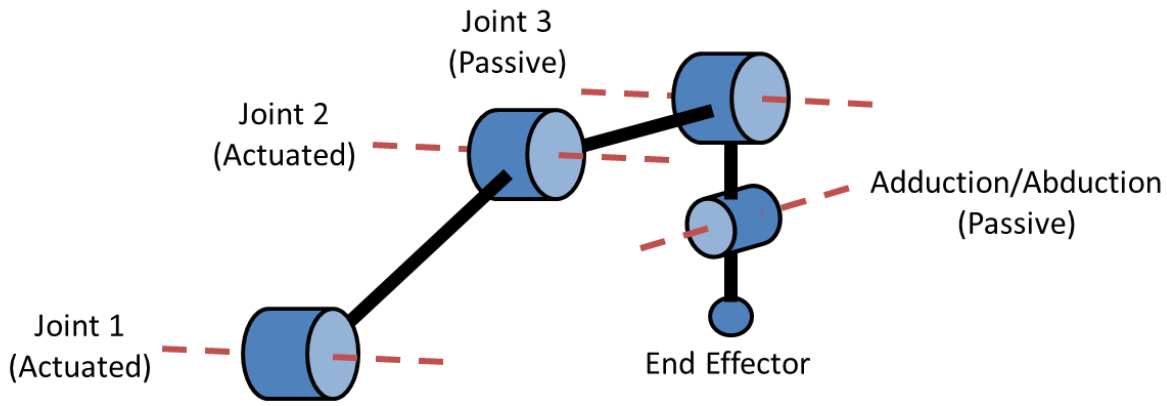

Figure 2.3: Kinematic Diagram Showing Manipulator DOFs.

These motions are not left entirely passive over sizeable angle ranges, as doing so would require longer third links to create space for the motions or additional bearings at the linkage bases. Both result in a larger and heavier device, so these options were forgone. For the thumb manipulator, adduction and abduction are neither actively controlled nor passive to any extent. However, the orientation of the base of the manipulator is adjustable, which allows the user to preset the degree of adduction and abduction prior to operation.

2.6 Accommodating Different Grasp Types

2.6.1 Interchangeable Finger Interfaces

A number of features of the exoskeleton allow the wearer to train different types of grasps, as opposed to only supporting a binary opening and closing of the hand. One such feature is the use of interchangeable end effector interfaces for the two finger manipulators. The finger interface is the portion of the third link that the user's fingers are strapped to. These finger interfaces are designed in multiple configurations in order to accommodate motions that require the four fingers to be grouped in a specific way. For example, a pinch requires one manipulator to control the index finger and the other manipulator to control the grouped middle, ring, and little fingers, while a thumb-2-finger grasp requires one manipulator to control the grouped index and middle fingers with the other manipulator controlling the grouped ring and little fingers. Figure 2.4 shows the four configurations of style interfaces that have been designed the exoskeleton.

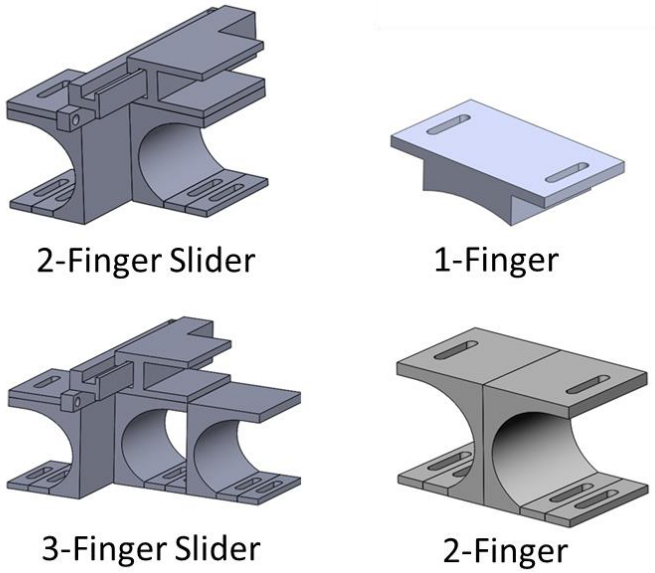

Figure 2.4: Styles of Finger Interfaces.

The 2-Finger Slider and 3-Finger Slider interfaces allow the ring and little fingers to slide relative to one another. Due to the large difference in length between these two fingers, the fingertips slide relative to one another during flexion and extension. The sliders accommodate this motion so that the fingers can move naturally during exercises.

2.6.2 Sliding Finger Manipulator Bases

The second feature that enables multiple grasps is sliding link bases for the finger manipulators, shown in Figure 2.5. This works in conjunction with the different finger groupings described above. Since the manipulators' end effectors are controlled in a plane, changing which fingers are controlled by each of the two manipulators necessarily requires these linkages' bases to be able to move laterally above the knuckles in order to avoid patient discomfort. For example, if one manipulator controls just the index finger, the manipulator can be slid such that it is directly above the index finger's MCP joint. The origin of the other manipulator, which controls the grouped middle, ring, and little fingers can be positioned around the MCP joint of the ring finger. Ruler markings on the side of the track on which the link origins slide allows the users of the exoskeleton to measure and record the positions of the link origins.

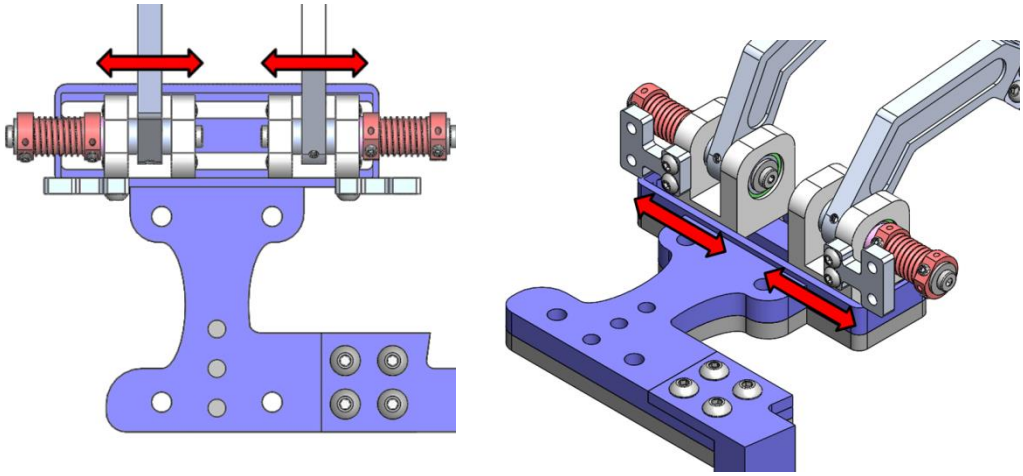

Figure 2.5: Sliding Link Origins.

2.6.3 Rotatable Thumb Manipulator

The third feature that supports different grasps is a rotatable thumb manipulator origin. The origin of the thumb linkage can be loosened, rotated to a certain desired angle in increments of 22.5°, and fixed at that angle before the user puts on the exoskeleton. The axis of rotation is depicted in Figure 2.6. This feature is necessary to maintain the desired trajectory for the thumb during exercises. The thumb of a stroke patient experiencing spasticity tends to default to a key grasp position. Therefore, fixing the thumb manipulator at different degrees of adduction and abduction allow the patient to practice other types of grasps.

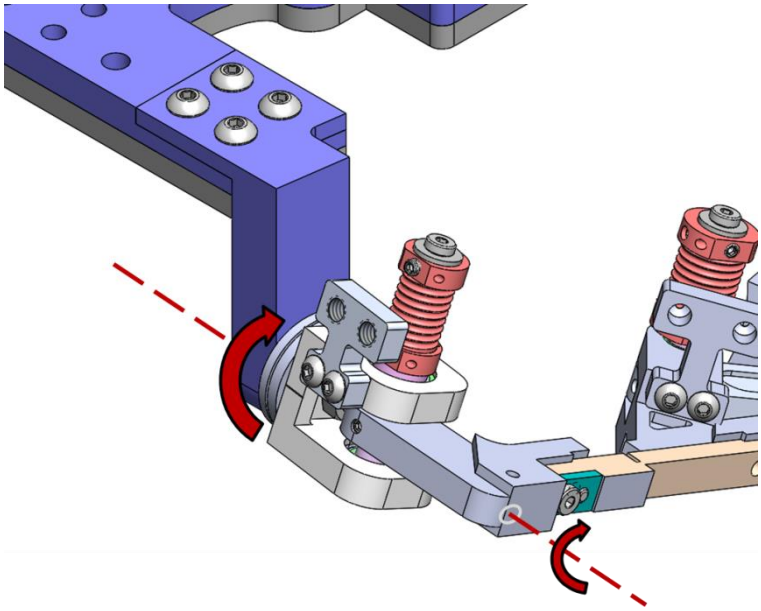

Figure 2.6: Rotatable Thumb Manipulator Origin

With the features presented above, this hand exoskeleton can assist a patient in performing various power and precision grasps, pinches, etc. Based on the taxonomy of grasps in [24], the user can perform the following:

- **Power grasps**
    - Lateral Pinch
    - The six prismatic grasps:
        - Large Diameter
        - Small Diameter
        - Medium Wrap
        - Adducted Thumb
        - Light Tool
- **Precision grasps**
    - Thumb-4 Finger

- Thumb-2 Finger
- Thumb-Index Finger

2.7 Accommodating Various Hand Sizes

Due to the variation in human hand sizes and the positioning of different anatomical features on the hands, it is important for an exoskeleton to be able to accommodate as many users as possible. The design objective here is for each linkage to accommodate the 95^{th} percentile hand. The hand measurements were taken from an anthropometry study involving United States Army personnel [24], and the 95^{th} percentile values for the male subjects were used. The dimensions that were most important during the design of the device were (i) the lengths, diameters, and breadths of the proximal, medial, and distal phalanges for each of the fingers, (ii) lengths, diameters, and breadths of first metacarpal, proximal phalanx, and distal phalanx for the thumb, and (iii) the overall length and breadth of the hand.

The sliding manipulator bases and finger interfaces described in the previous section also contribute to accommodating hands of various sizes. The sliding manipulator bases allow the manipulators to be positioned above the appropriate knuckles, the positions of which will vary depending on the size of the user's hand. The sliding finger interfaces allow hands to fit the interfaces regardless of the variability in the difference in length of the ring and little fingers.

Another advantage of the interchangeable finger interfaces is that they are made of ABS plastic and be 3D printed. This allows for the quick creation of interfaces of various sizes, thicknesses, and curvatures. In this way, patients with particularly thin or thick fingers will still have an interface that their fingers can fit into comfortably.

In order to ensure that the manipulators can reach any point within the workspace of a 95^{th} percentile finger, the appropriate link lengths had to be chosen. In order to find the desired balance between workspace coverage, link stiffness, and manipulator length, an optimization was run to determine the link lengths for each manipulator. This optimization is detailed in the following chapter, and a case study of the index finger manipulator is presented.

2.8 Actuation

The exoskeleton is actuated by a motor pack separate from the hand. The actuator pack itself will be mounted on an existing component of the EXO-UL7. This fulfills the design requirement that the manipulators be remotely actuated. Power is transmitted from the actuator pack to the manipulator joints through a system of capstans and Bowden cables. A CAD rendering of the uncovered actuator pack is shown in Figure 2.7. During operation, this pack is covered with a 3D-printed ABS shell for protection.

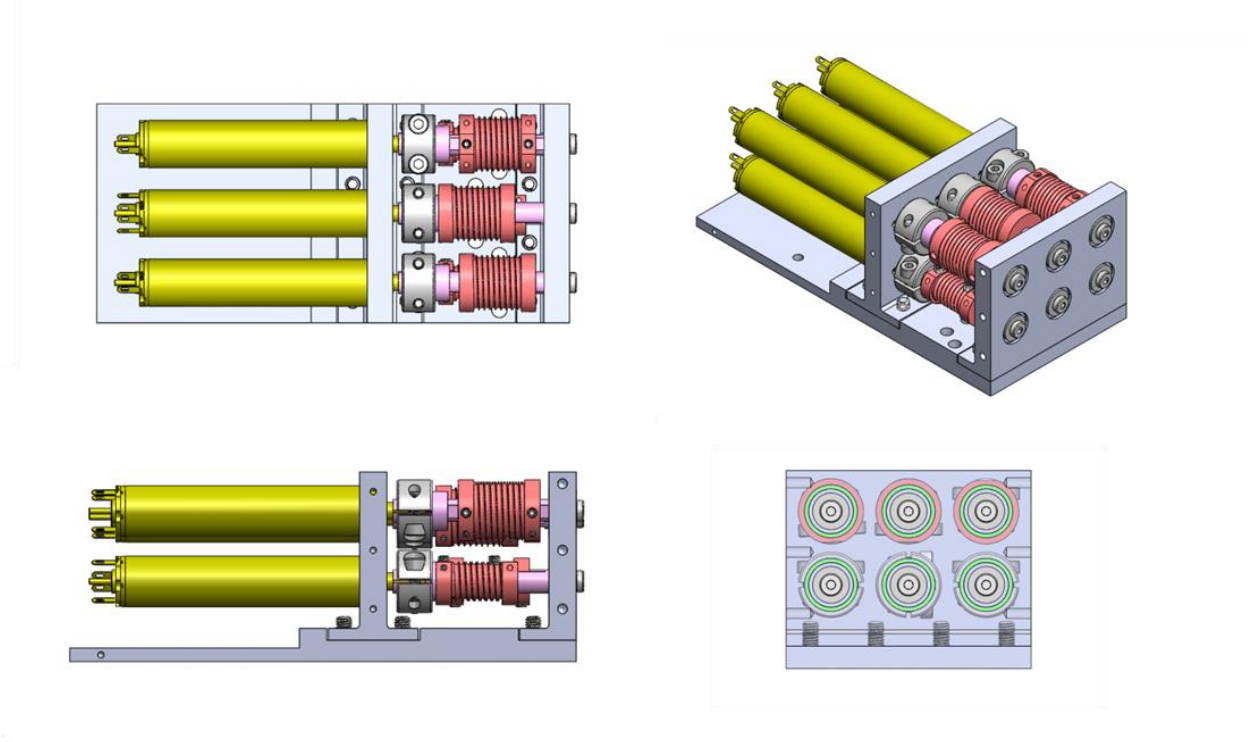

Figure 2.7: Uncovered Actuator Pack.

There are two main advantages to using such a system. The first is that it allows for flexible and unpredictable routing of the cables. Throughout operation, the hand will be opening and closing, and the user will be moving the entire hand itself relative to the actuator pack. The flexible sheathing system is capable of accommodating curved paths in 3D space. The second advantage is that this system maintains constant tension despite the user moving the device. With fixed attachment points and a fixed sheath length, the sheath will bend and adjust the path between the actuator pack and the manipulator joints such that the distance the cable travels is constant (provided that the path is not longer than the sheathing itself).

The disadvantages of the Bowden cable actuation system is that it is subject to friction between the sliding cable and the inner material of the sleeve. This friction is complex and varies with bend angle and overall cable tension [25]. Bowden cable systems are also susceptible to

backlash as the cable slides within the sheath. To address these limitations, the actuator pack motors have been oversized to ensure that frictional losses do not result in the manipulator joints receiving insufficient torque from the motors, and the difference between the cable diameter and the inner diameter of the sheathing have been minimized.

The cable chosen is stainless steel of 7x49 construction with a breaking strength of 170lbf. The 7x49 construction allows for maximum flexibility. The high breaking strength was chosen for three reasons. Firstly, it gives the power transmission system a large safety factor relative to the grasp strength of a human hand to prevent failure. This safety factor also takes into account the fact that a cable that must adhere to the curve around a capstan does not achieve 100% of its breaking strength while straight. Secondly, its durability helps alleviate the need to change cables frequently. And thirdly, this cable and its high breaking strength have a correspondingly large diameter (0.044”), which fits into the inner diameter of the conduit (inner diameter of 0.072”) such that smooth motion is maintained while minimizing backlash.

The actuators used for each joint are Maxon RE13 motor combinations with a maximum output torque of 2.0 Nm. From Figure 2.7, it can be seen that capstans attached to the upper row of motors are larger, with 14mm diameters, than the capstans on the bottom rows, with 9mm diameters. This was done to allow the motors to be in this compact “stacked” configuration without the cables from the top capstans interfering with those on the bottom row. As a consequence, however, the joints actuated by the bottom row of motors receive only a fraction of the motors’ output torques according to

$$\tau_{\text{joint}} = \frac{d_{\text{joint capstan}}}{d_{\text{motor capstan}}} \tau_{\text{motor}} \tag{2.1}$$

By (2.1), the aforementioned joints have a maximum output torque of 1.28 Nm. Therefore, these motors control Joint 2 of the manipulators.

2.9 Sensors

The force exerted by the user's finger(s) on the end effector is taken as the input to the control system, which will be discussed in a later chapter. To sense the force, each of the three manipulators has a bending beam load sensor (FUTEK Advanced Sensor Technology, Inc.) incorporated into one of the links of the manipulator. For the finger manipulators, the force sensor is part of the second link. The second link is chosen for the sake of proximity to the end effector and for ease of calculating the end effector force based on the joint angles read by the system's encoders. For the thumb manipulator, the bending beam load sensor is incorporated into the first link of the manipulator. Through experimenting with physical prototypes, it was found that making the sensor part of the second link prevented the thumb linkage from being made as compact as possible. Therefore, it was made part of the first linkage, which had the longest overall length. Figure 2.8 shows how these sensors are implemented into the links.

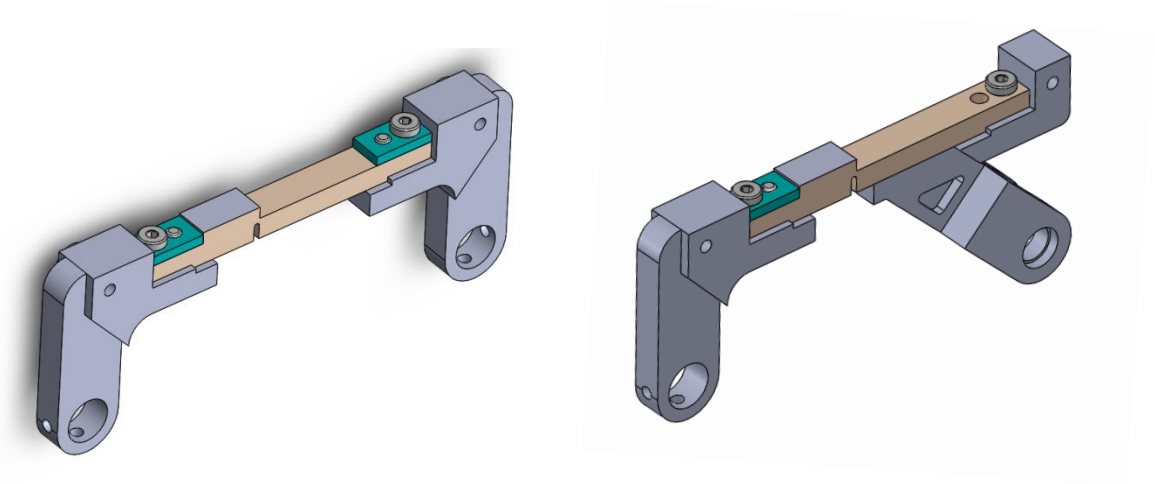

Figure 2.8: Sensor links for the finger manipulators (left) and thumb manipulator (right).

The active joints of the manipulators are sensed by encoders attached to the joint motors and gearboxes (Maxon). The passive joint of the manipulator is sensed using a magnetic incremental encoder (Renishaw, Inc.).

CHAPTER 3

Link Length Optimization

3.1 Introduction

This chapter details the optimization method used to determine the link lengths of the two finger manipulators and the thumb manipulator of the hand exoskeleton. First, the objective of the optimization is described. Following this, the models of the manipulator and the fingers are detailed. Finally, the algorithm is run and the results are interpreted in detail for the index finger manipulator of the exoskeleton.

Recall that the goal is for the device to accommodate a variety of hand sizes with fixed link lengths and achieve the best kinematic performance within the desired workspace. The optimization strategy is focused on both kinematics and workspace coverage. In contrast, previous work in optimization for hand exoskeletons has focused on maximizing torque transmission on the fingertip being manipulated [26], [27]. First, the algorithm and the method by which it grades each potential mechanism are presented. Second, models for both the mechanism and the finger(s) of interest are described. The specific case of the index finger manipulator is run. Finally, the theoretically optimal solution from the algorithm is compared to the actual mechanism, which was physically realized as a physical prototype and experimentally optimized under various constraints.

3.2 The Optimization Algorithm

The overall objective is to determine the set of manipulator link lengths that will give the best kinematic performance within the workspace of the finger. The methodology behind the optimization is as follows. The algorithm receives as inputs the variables for the potential link lengths L_1, L_2, and L_3. The algorithm will go through all of the different combinations of link lengths and for each calculate a design score based on parameters that will be discussed in this section. Via this brute force method, the theoretically optimal design is determined. Following the calculations, there are a few criteria that will automatically invalidate a design if they are not met.

The first criterion is overlapping workspace area. The workspace of the manipulator must completely overlap the workspace of the finger, i.e., the end effector of the manipulator must be able to reach anywhere the fingertip could move. To address this, the algorithm will calculate the boundary and size of both workspaces to ensure that they overlap completely. The second criterion is inverse kinematics. If the inverse kinematics solutions for the manipulator do not exist for all points in the finger's workspace, the design is invalidated. The third criterion is interference between the manipulator links and the finger. If the inverse kinematics solution for the set of potential link lengths shows that in order to reach the fingertip, a joint of the manipulator must lie within the flesh of the finger, the design is marked as unacceptable, as this indicates there would be interference between the user and the manipulator links.

First, the algorithm calculates the workspace of the *smallest* finger that will be manipulated by the linkage, as this finger is the one that limits the motion of the other fingers, if any, that are also attached to the end effector. For one finger manipulator, the smallest finger will always be the index finger, and for the other manipulator, it will always be the little finger. For a potential

set of manipulator link lengths (L_1, L_2, L_3), the mechanism isotropy is determined for the joint spaces that position the end effector within the workspace boundary of the finger. The information obtained from this process is used to calculate a design score for the potential set of link lengths. This process is then repeated for all combinations of links within a certain size range for each link in the manipulator. Evaluating this data for both finger manipulators and the thumb manipulator yields the theoretically optimal link lengths for the exoskeleton.

3.2.1 The Design Score

One component of the design score is kinematic performance. The analysis in the optimization uses the mechanism isotropy (ISO) performance measure as one parameter in the design score, which grades each potential mechanism. Mechanism isotropy is a measure of the ability of a mechanism to move its end effector in any direction. It is a function of the joint angles $(\theta_1, \theta_2, \theta_3)$ and ranges from 0 to 1. Mechanism isotropy can be defined as in [28] as

$$\mathrm{ISO}(\theta_1, \theta_2, \theta_3) = \frac{\lambda_{\min}}{\lambda_{\max}} \in \langle 0, 1 \rangle \tag{3.1}$$

where $\lambda_{\min}$ and $\lambda_{\max}$ are the minimum and maximum eigenvalues of the Jacobian matrix. An isotropy value of zero indicates a singularity and the loss of a degree of freedom, while an isotropy of 1 indicates that the end effector can move equally well in all directions.

Potential mechanisms should have an increase in design score in accordance with higher mechanism isotropy values within the finger workspace. One way to incorporate isotropy into the score is by summing isotropy values over the finger workspace. Let K be defined as the set

containing the discrete points within the finger workspace that have been calculated. Each calculated point has an associated isotropy value. In finding the sum of the mechanism isotropy within the workspace, an adjustment must be made to account for varying densities of calculation points in K. To address this, the finger workspace area is discretized into a grid of cells along the x- and y-directions. The average mechanism isotropy is calculated within each of these cells and multiplied by the cell's area. The sum total of all the cells' area-weighted values is taken as the sum of isotropy. A potential mechanism is rewarded for having a higher sum of isotropy.

If there is a position where the isotropy is zero within the finger workspace, the design score should be zero as well because this indicates a singularity. A potential mechanism should also have a higher design score for having a higher minimum mechanism isotropy value within the workspace compared to other sets of link lengths. These requirements are reflected in the numerator of the equation for design score.

Another factor to consider in the design score is that although larger links tend to lead to better system isotropy values within the workspace, they also result in the mechanism having greater mass and lower mechanism stiffness, which are unfavorable. Additionally, long link lengths increase the size of the envelope of the mechanism above the wearer's hand. This increases the potential for interference occurring between the linkages and surrounding objects or other parts of the exoskeleton during therapeutic exercises. Therefore potential designs should be penalized for being too large. Beam theory shows that mechanism stiffness is inversely proportional to the cube of the sum of the link lengths. Including this in the expression gives the final design score equation.

$$\text{Design Score} = \frac{\sum_K \text{ISO}(\theta_1, \theta_2, \theta_3) * \text{MIN}_K(\text{ISO}(\theta_1, \theta_2, \theta_3))}{(L_1 + L_2 + L_3)^3} \tag{3.2}$$

With these quantities of interest in mind, both the manipulator and finger are modeled in the following sections.

3.3 Modeling the Manipulator

Recall from the previous chapter that each of the exoskeleton's manipulators is a 3R planar mechanism. For a general 3R planar mechanism, the only nonzero Denavit-Hartenberg parameters correspond to all three of the link lengths and their joint angles. Table 3.1 shows a complete listing of the DH parameters.

Table 3.1: DH Parameters for 3R Planar Mechanism

$i-1$	i	α_{i-1}	a_{i-1}	d_i	θ_i
0	1	0	0	0	θ_1
1	2	0	L_1	0	θ_2
2	3	0	L_2	0	θ_3
3	4	0	L_3	0	0

The position of the end effector is described by a two coordinates (x,y) and orientation ϕ. The forward kinematics equations are given in (3.3).

$$\begin{bmatrix} x \\ y \\ \phi \end{bmatrix} = \begin{bmatrix} L_1 c_1 + L_2 c_{12} + L_3 c_{123} \\ L_1 s_1 + L_2 s_{12} + L_3 s_{123} \\ \theta_1 + \theta_2 + \theta_3 \end{bmatrix} \tag{3.3}$$

where

$s_1 = \sin\theta_1$, $s_{12} = \sin(\theta_1 + \theta_2)$, $s_{123} = \sin(\theta_1 + \theta_2 + \theta_3)$

$c_1 = \cos\theta_1$, $c_{12} = \cos(\theta_1 + \theta_2)$, $c_{123} = \cos(\theta_1 + \theta_2 + \theta_3)$.

The forward kinematics yield the Jacobian matrix with respect to the ground frame as

$$^0J = \begin{bmatrix} -L_1 s_1 - L_2 s_{12} - L_3 s_{123} & -L_2 s_{12} - L_3 s_{123} & -L_3 s_{123} \\ L_1 c_1 + L_2 c_{12} + L_3 c_{123} & L_2 c_{12} + L_3 c_{123} & L_3 c_{123} \\ 1 & 1 & 1 \end{bmatrix} \quad (3.4)$$

However, using this 3x3 Jacobian matrix where every entry in the third row is 1 results in a matrix that can give negative minimum eigenvalues and positive maximum eigenvalues. The ratio of these yields negative numbers, which do not fit into the isotropy measure, which is bounded by 0 and 1. If we instead take the two rows corresponding to the x- and y- coordinates as a 2x3 matrix, we can instead look to the singular values of the matrix J^TJ. Taking q to be the position vector of the end effector and θ as the column vector of joint angles gives

$$\dot{x} = J\dot{\theta}$$

$$x^T * x = \dot{\theta}J^T * J\dot{\theta}$$

From a singular value decomposition of the Jacobian as $J = V^T\Sigma U$, this becomes

$$x^T * x = \dot{\theta}(U^T\Sigma V) * (V^T\Sigma U)\dot{\theta}$$

U and V are unit matrices, giving:

$$U^TU = 1 \text{ and } V^TV = 1$$

$$x^Tx = \dot{\theta}(U^T\Sigma * \Sigma U)\dot{\theta} \quad (3.5)$$

From (3.5), we see that $J^T J$ and $\Sigma * \Sigma$ are similar, and the eigenvalues of $J^T J$ are the squares of the singular values of the original Jacobian matrix J. Therefore, these values are used to calculate mechanism isotropy.

The inverse kinematics for the 3R planar mechanism are given in (3.6)-(3.8) . These equations are used in the optimization to check that the joints of a potential design do not interfere with the flesh of the finger itself when the finger is in the clenched position.

$$\theta_1 = \gamma \pm \sigma \operatorname{acos}\left(\frac{-(x_p^2 + y_p^2 + L_1^2 - L_2^2)}{2L_1\sqrt{x_p^2 + y_p^2}}\right) \text{ (elbow up/down)} \tag{3.6}$$

$$\theta_2 = \operatorname{atan2}\left(\frac{y_p - L_1\sin(\theta_1)}{L_2}, \frac{x_p - L_1\cos(\theta_1)}{L_2}\right) \tag{3.7}$$

$$\theta_3 = \phi - \theta_1 - \theta_2 \tag{3.8}$$

where

$$x_p = x - L_3\cos(\phi)$$

$$y_p = y - L_3\sin(\phi)$$

$$\gamma = \operatorname{atan2}\left(\frac{-y_p}{\sqrt{x_p^2 + y_p^2}}, \frac{-x_p}{\sqrt{x_p^2 + y_p^2}}\right)$$

$$\sigma = \pm 1.$$

3.4 Modeling the Finger

The index finger is also modeled as a 3R planar mechanism, and the same kinematics equations will apply. Each relevant joint and bone in the anatomy corresponds to a joint and link in the finger mechanism model. For the fingers, this mechanism starts from the MCP joint (Joint 1),

along the proximal phalanx (Link 1) to the PIP joint (Joint 2), along with medial phalanx (Link 2) to the DIP joint (Joint 3), and along the distal phalanx (Link 3) to the fingertip. For this optimization we use the lengths of the phalanges to be those in the 95th percentile for each bone. The proximal, medial, and distal phalanges are taken to be $L_1 = 2.79$ in, $L_2 = 1.06$ in, and $L_3 = 1.27$ in, respectively [23]. The joint ranges used for each potential mechanism in the optimization calculation are listed in Table 3.2.

Table 3.2: Joint Ranges for Potential Manipulators

Joint	Range
1	$\theta_1 \in [-80°, 150°]$
2	$\theta_2 \in [-160°, 0°]$
3	$\theta_3 \in [-170°, 0°]$

The hand exoskeleton will physically interface with the dorsal side of the wearer's hand via a modified glove. The material and form factor of the glove, along with the physical interface between the fingertip and end effector of the manipulator, restrict the finger from reaching the entirety of its uninhibited workspace. To account for this, multiple angle ranges are defined for each of Joints 1 through 3. These angle ranges are used during the optimization in determining the finger workspace. Each joint has a "primary range", which can be used to describe most of its positions. Each joint also has a "restricted range", within which the range of the next joint is restricted to its "secondary range". This information is summarized in Table 3.3. These angle ranges were obtained through observations while wearing the aforementioned glove.

Table 3.3: Joint Ranges for Index Finger Model

Joint	Primary Range	Secondary Range	Restricted Range
1	$\theta_1 \in [-90°, 45°]$	-	$\theta_1 \in [-90°, -80°]$
2	$\theta_2 \in [-120°, 0°]$	$\theta_2 \in [-100°, 0°]$	$\theta_2 \in [-90°, 45°]$
3	$\theta_3 \in [-90°, 5°]$	$\theta_3 \in [-70°, 0°]$	-

3.5 Optimization Results and Discussion

3.5.1 Comparison of Theoretical and Experimental Values

Figure 3.1 shows a plot of the design scores for the range of interest of $L_1 \in$[3in,5in], $L_2 \in$[1in,3in], $L_3 \in$[3in,5in]. These are the design scores for all possible combinations of link lengths within the given range. Due to a sensor to be included in the second link of the manipulator in the actualized hand exoskeleton, we must impose the constraint that $L_2 = 3.5$ in. Therefore, the relevant subset of data from Figure 3.1 is the plane of $L_2 = 3.5$ in. The design scores on this plane are displayed in Figure 3.2. The white data points on this contour plot mark the only link length combinations within this plane that are actually acceptable based on the criteria of workspace overlap, inverse kinematics, and joint interference as described in the previous section.

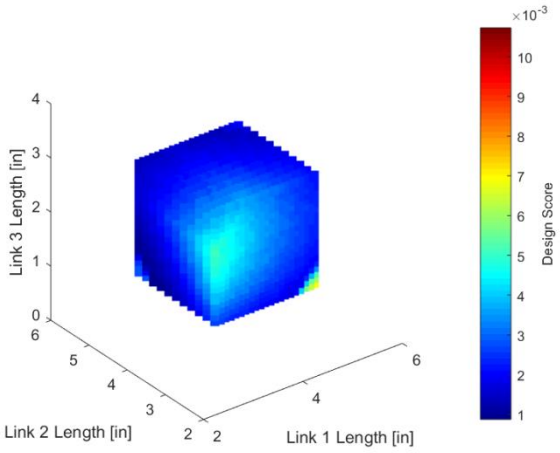

Figure 3.1: A 3D plot showing a color map of design scores for sets of potential manipulator link lengths (L_1, L_2, L_3).

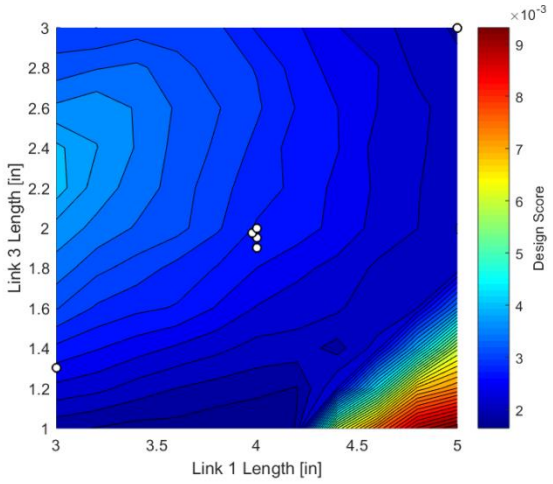

Figure 3.2: Contour plot of design score at the plane L_2 = 3.5in. White data points mark the acceptable designs in the plane.

As seen in Figure 3.2, the design score "hot spot" lies towards the bottom right corner of the contour plot where L_1 is at the highest within the data range and L_3 is at its lowest. Of the acceptable designs, the one with the highest design score, i.e. the one closest to this area of

interest, is the one the algorithm has determined to be the optimal one. This set of link lengths is L_1 = 4.0 in, L_2 = 3.5 in, L_3 = 1.95 in.

The manipulator linkage for the index finger was realized as a physical prototype as shown in Figure 3.3. This rapid prototype was created with adjustable links to size the entire linkage as appropriate to the authors' hands. The objective of this was to experimentally adjust and shape the links to make them as short as possible while maintaining smooth movement, ensuring total workspace coverage, and avoiding singularities within the workspace and interference between the links and the index finger. This results in the set of experimentally optimized link lengths of L_1 = 3.0 in, L_2 = 3.5 in, and L_3 = 1.3 in.

Figure 3.3: Physical prototype of the index finger manipulator with experimentally adjusted link lengths.

The comparison between the theoretically optimal set of linkages as determined by the algorithm and the experimentally optimal links are shown in Table 3.4. These algorithm results are marked as "Theoretical Unweighted", the reason for which is addressed in a section to follow. The values in parentheses are the percent differences between the actual and theoretical values of various quantities of interest.

Table 3.4: Comparison Between Algorithm Results and Physical Prototype (Index Finger)

	L_1	L_3	Sum of Isotropy Within Workspace	Minimum Isotropy Within Workspace	Cube of Sum of Link Lengths	Design Score
Experimental	3.00	1.75	22.76	0.0801	561.5	0.00325
Theoretical Unweighted	4.00 (-25.0%)	1.95 (-10.3%)	29.11 (-21.8%)	0.0785 (2.1%)	843.9 (-33.5%)	0.00271 (19.9%)
Theoretical A=1, B≥3.75	3.00 (0%)	1.30 (34.6%)	20.89 (8.9%)	0.0531 (50.7%)	474.6 (18.3%)	0.00234 (38.8%)

The experimental values for L_1 and L_3 are lower than those produced by the optimization by 25.0% and 10.3% respectively. The sum of isotropy is lower by 21.8%, while the minimum isotropy value is greater by 2.1%. A potentially confusing result is that the design score is greater than the one predicted to be optimal by 19.9%.

There are two main factors that contribute to these differences between the theoretical and actual values for the link lengths. The first is the fact that the optimization algorithm and the experimental optimization were performed for *different* hand sizes. As mentioned in a previous section, the optimization code used a model finger comprised of proximal, medial, and distal phalanges which were all of the 95^{th} percentile in length in order to ensure that the manipulator would be able to accommodate as many individuals as possible. According to [23], a finger with such phalanges would have an overall length that lies above the 99^{th} percentile. In contrast, the experimental adjustment of the links was done in accordance with the authors' fingers, which fall within the 95^{th} percentile for overall length as opposed to the 95^{th} percentile in length for each individual phalanx. With this in mind, the conceptual expectation is that the link lengths obtained experimentally are smaller than the ones obtained through the optimization. Therefore, it is expected that the theoretically optimized manipulator is larger than the manipulator created via a

physical prototype, and this is the case. Because the design score is inversely proportional to the cube of the sum of the link lengths, this fact results in a design score that is higher than that of the theoretical set of link lengths. One may ask why the design obtained experimentally was not predicted by the algorithm as the optimal one if it has a higher design score. The explanation for this is that this shorter set of link lengths was marked as unacceptable due to the algorithm, as these shorter links do not have solvable inverse kinematics without any joint interference for the larger finger used in the optimization.

The second factor contributing to the differences between our theoretical and experimental values is the difference in priorities between the algorithm and the experimental optimization. The original design score equation in (3.2) weighs each of the terms related to isotropy equally, and the sum of the cube of the link lengths three times as much. However, when the links were experimentally adjusted, the highest priority was making the link lengths as small as possible, provided that the manipulator's movement still felt uninhibited within the finger workspace. This fact introduces a more subjective aspect to the design process that the original design equation does not account for. The particular emphasis on reducing link size is not reflected in (3.2).Therefore there is a disagreement between the design priorities of the algorithm and our own objectives while working with the prototype.

3.5.2 Modified Design Score Equation

A variation of the design score equation can be developed to include weight factors that allow for the flexibility of increasing or decreasing the relative importance of the design score equation's components. This is modified equation is expressed as

$$\text{Design Score} = \frac{[\sum_K ISO(\theta_1, \theta_2, \theta_3) * \text{MIN}_K(ISO(\theta_1, \theta_2, \theta_3)]^A}{[(L_1 + L_2 + L_3)^3]^B} \quad (3.9)$$

where A and B are the weight factors for the isotropy terms and the link size terms, respectively.

Figure 3.4 shows plots of design score in the plane where L_2 = 3.5 in that result from increasing the weight factor B, which increases the importance of link size in the design score. As B increases, the original hot spot region for design score fades while the region with lower L_1 and L_3 emerges as the new hot spot. This transition between hot spots takes place when the weight factor for link size B = 3.75. It follows that the acceptable design with the highest design score according to (3.9) becomes L_1 = 3.0 in L_2 = 3.5 in, and L_3 = 1.3in. The bottom row of Table 3.4 shows the comparison of percent differences in the design score equation with the weight factors. The 34.6% difference between L_3 values methods can explained by physical constraints in the construction of the prototype. Specifically, in order to ensure that the proper degrees of freedom are present in the physical mechanism, the third link requires two rotation axes. Due to the amount of space these axes require, L_3 = 1.75 in is the limit to how small the third link can physically be. Overall however, the approach using weight factors leads to greater agreement between the results of the optimization algorithm and the experimental adjustment of the physical prototype.

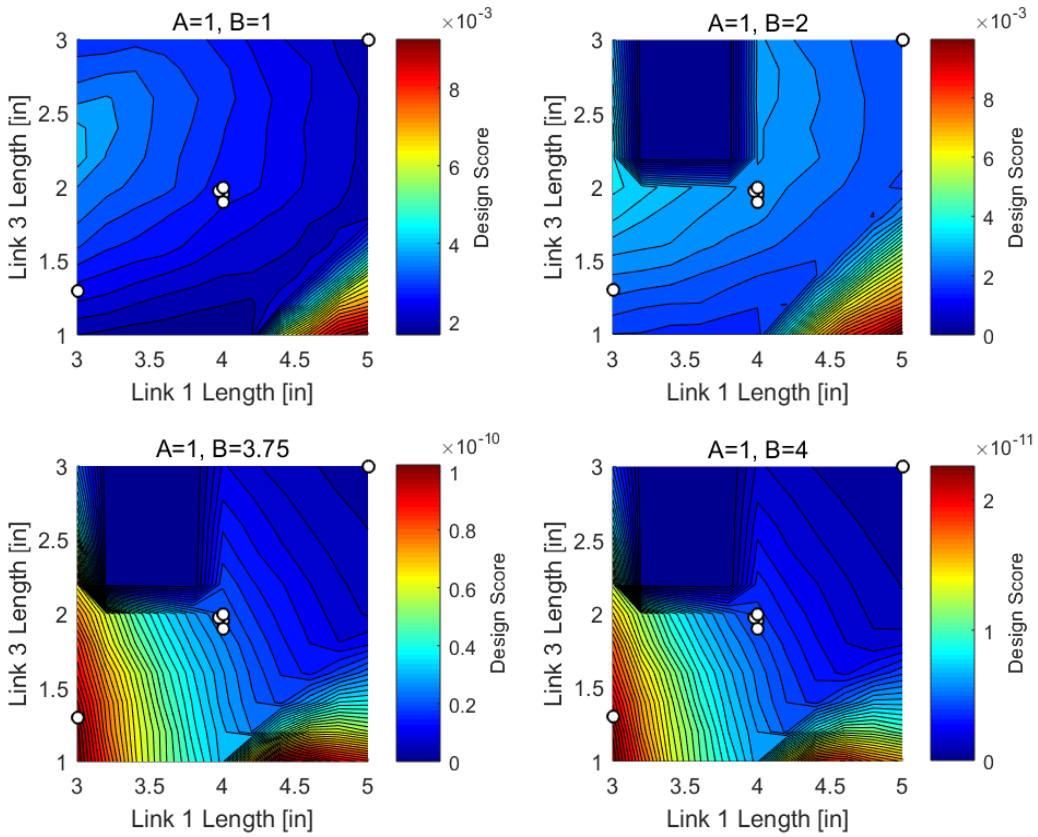

Figure 3.4: Contour plots showing the influence of weight factors on hot spots of high design scores.

As expected, increasing the weight factor B beyond the point at which the two hot spots have equal design scores results in the emergent hot spot overtaking the old one. This is illustrated in Figure 3.4 with A = 1 and B = 2. Conceptually, increasing B more beyond this point results in smaller and smaller links being favored. This makes sense both mathematically and physically. Mathematically, the denominator of (3.9) becomes unboundedly large as B increases, and the denominator of the design score equation increases accordingly much faster than the isotropy terms in the numerator could limit it. This continues until an inevitable singularity occurs due to these now smaller links trying and being unable to reach the boundaries of the

workspace of the finger. This sets the design score to zero where the emergent hot spot is when B = 3.75, ultimately creating a "cold spot" beyond which any link length combinations are unacceptable. In terms of the physical prototype and finding this result intuitively and through experiment, this corresponds to the situation in which smaller link lengths were favored much more compared to the tactile "smoothness" of the mechanism's movement. The links would become smaller and smaller until they could no longer physically reach where the experimenter's hand attempts to go. This, along with any smaller link combinations, limits the motion of the experimenter's hand, and the set of link lengths would be deemed unacceptable. Thus, the shortest acceptable set of link lengths would be reached both mathematically through the algorithm and physically through experimentation.

In addition to causing a new hot spot to emerge, the addition of weight factors to the design score also causes the creation of a sizeable cold spot within the plane. This rectangular cold spot is in the region where L_1 is small and L_3 is large, and it is seen in Figure 3.4 in the subplots with $B \geq 2$.When A = 1 and B = 1, the plane of design score values can be seen as relatively flat with no deep wells. The most interesting feature is located at the area surrounding the hot spot with large L_1 and small L_3. In this lower-right region of the plot, the design score changes quickly over small changes in link length. However, as link length is weighted more heavily, the topology of the map changes. In addition to there being a greater number of contour lines in the area nearby the hot spot, the aforementioned cold spot is created, around which there is a steep drop in design score. Physically, one interpretation of this is that any increase in the mechanism isotropy terms caused by decreasing L_1 and increasing L_3 (which is one direction of increasing design score until the cold spot is suddenly reached) is quickly negated and overwhelmed by the benefit to link length reduction gained from decreasing L_1. This is due to the fact that the first

link is the longest link in the manipulator and thus influences the denominator of the design score equation much more than the other two links.

Another striking graphical effect worth interpreting is the rearrangement of the contour lines with increasing weight factor B. For B = 1, the contour lines indicate that design score increases with increasing L_1 and decreasing L_3. This reflects how physically, a large L_1 results in smooth mechanism movement, increasing the isotropy terms in the design score equation. The same pattern holds for the case with B = 2. However, as the new hot spot emerges with $B \geq 3.75$, the contour lines rearrange to indicate that the design score increases as both L_1 and L_3 decrease. This new direction of increase is visually almost perpendicular with the one from the cases where link length was not prioritized as heavily. At this point, the weight factors A and B are adjusted such that the plot suggests that the way to achieve the optimal design is to decrease both link lengths as much as possible without the mechanism reaching a singularity or failing to cover the entire finger workspace. This is in direct agreement with the main design objective we worked towards during the experimental determination of the optimal link lengths. Therefore, the direction of increasing design score as shown by the contour lines is an important feature in the plots that can be used to judge whether or not the design score equation in the algorithm is in agreement with the strategy driving the experimental optimization.

3.6 Future Applications of the Algorithm

Although this study presents a specific case in which a 3R planar manipulator is the mechanism of interest, the methodology behind the optimization could easily be applied to any other type of mechanism in which an end effector must control a body part that interfaces with it at a fixed point, provided that the kinematics and inverse kinematics are solvable. The weight factors used in this optimization make the design score equation flexible to fit the priorities of the designers.

Improvements that can be made to this method in the future include optimizing the mechanism towards specific regions within the desired workspace. For instance, statistics may show that a hand spends most of its time during activities of daily life in certain clenched positions. These positions can be mapped to a region within the overall workspace of the fingers, and the design score equation and weight factors can be modified to prioritize kinematic performance in these particular areas. The same principle can be applied to optimize performance in workspaces areas where stroke patients with spasticity have particular difficulty moving.

3.7 Summary

In this chapter, the optimization method used that was used as a tool to determine the optimal link lengths for the hand exoskeleton manipulators was presented. Potential mechanisms were graded with a design score that focuses on the kinematic performance measure of mechanism isotropy, was well as mechanism stiffness. The specific case of using this algorithm to optimize the index finger manipulator was presented in detail, and the results of the algorithm were compared to the results obtained via experimentation with a physical prototype. The differences between the results were explained in the context of the parameters entered into the algorithm and the matching of the algorithm's priorities with those of an experimenter optimizing the manipulator physically. The addition of weight factors to the design score was explored as a means of reconciling any differences between the algorithm's grading of each potential mechanism and the objectives held when obtaining the optimal link lengths experimentally.

CHAPTER 4

Control System

4.1 Admittance Control

An admittance control scheme is used to control the hand exoskeleton. If the force at the end effector of the manipulator is taken to be the mechanical analog to voltage, and the velocity of the end effector is taken to be analogous to current, a mechanical analog to electrical admittance is drawn. In admittance control, the relationship between the force exerted on the end effector by the exoskeleton's user and the motion of the end effector is controlled. In particular, this exoskeleton uses joint space admittance control. That is, the force of the user's fingers are converted into joint torques in the manipulator, which are then used to calculate the new joint angle set points in the end effector's trajectory. These joint trajectories are then followed using a PID controller. The control system is carried out using an NI myRIO device, and the control scheme is coded in LabVIEW.

Before describing the details of the control scheme itself, first the nature of the controls of the manipulator are defined. As discussed previously, the manipulator is a 3R planar manipulator. The links' coordinate frames are defined as shown in Figure 4.1, which also shows the force exerted by the user's fingers on the end effector.

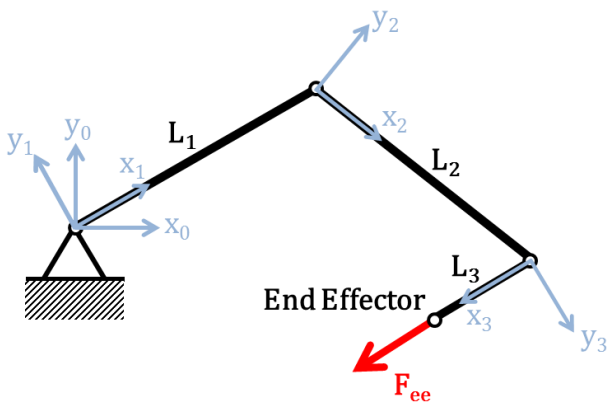

Figure 4.1: Coordinate Frames of the Manipulator

As a result of the third joint being passive and the nature of how the finger interfaces with the third link, the force exerted by the user is always in line with the third link. The bending beam load sensor link, Link 2 for the finger manipulators, senses the component of the end effector force that is perpendicular to the sensor. Using the angle information from the encoders, this force can be used to determine the force at the end effector with respect to the "ground" frame of the device. Figure 4.2 shows joint angles along with the end effector force. Figure 4.3 shows the end effector force vector along with the component measured by the sensor on Link 2.

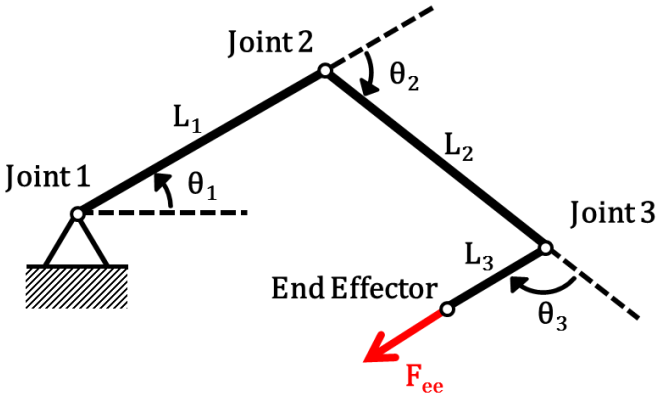

Figure 4.2: Definition of Joint Angles for the Manipulator

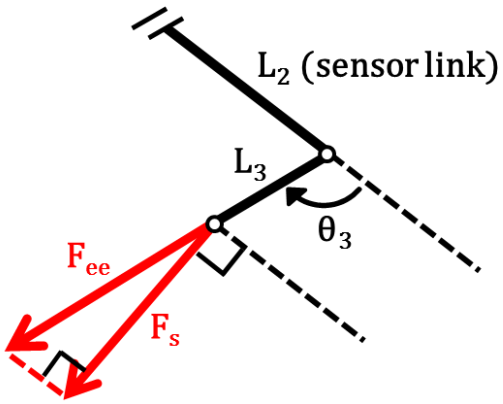

Figure 4.3: Component of End Effector Force Perpendicular to Sensor

The force F_s read by the sensor can be expressed in reference frame 3 as

$$F_s = F_{ee}\sin(\theta_3) \tag{4.1}$$

Therefore, the force at the end effector of the finger manipulator as expressed in frame 3 is

$${}^3F_{ee,fingers} = \begin{bmatrix} \dfrac{F_s}{\sin(\theta_3)} \\ 0 \\ 0 \end{bmatrix} \tag{4.2}$$

For the thumb manipulator, which has the sensor on the first link, the force at the end effector as expressed in frame 3 is

$$F_s = F_{ee}\cos(\theta_2 + \theta_3 - 90°) = F_{ee}\sin(\theta_2 + \theta_3) \tag{4.3}$$

$${}^3F_{ee,thumb} = \begin{bmatrix} \dfrac{F_s}{\sin(\theta_2 + \theta_3)} \\ 0 \\ 0 \end{bmatrix} \tag{4.4}$$

Based on the joint angles in Figure 4.1, the rotation matrix relating reference frame 3 and the ground frame of the exoskeleton is:

$$ {}^{0}_{3}R = \begin{bmatrix} c_{123} & -s_{123} & 0 \\ s_{123} & c_{123} & 0 \\ 0 & 0 & 1 \end{bmatrix} \tag{4.5} $$

where $c_{123} = \cos(\theta_1 + \theta_2 + \theta_3)$ and $s_{123} = \sin(\theta_1 + \theta_2 + \theta_3)$. In general, the end effector force in the hand exoskeleton ground frame is then:

$$ {}^{0}F_{ee} = {}^{0}_{3}R \ {}^{3}F_{ee} \tag{4.6} $$

This is the force that is taken to be the input to the admittance control algorithm.

As discussed in a previous chapter, only Joints 1 and 2 are actuated, while Joint 3 is passive. Therefore from the perspective of the control algorithm, the manipulator is a 2R planar mechanism consisting of the first and second links. This means that the position of the end effector is controlled to be within a circle (or, due to the links' physical constraints, a semicircle) of radius equal to the length of the third link L_3. Although the angle of the third link is not controllable, it is still sensed and is used to calculate the position of the end effector. This is useful for determining the end position of the fingertip during rehabilitation exercises. The forward kinematics and Jacobian of the 2R planar mechanism are given by:

$$ \begin{bmatrix} x \\ y \end{bmatrix} = \begin{bmatrix} L_1 c_1 + L_2 c_{12} \\ L_1 s_1 + L_2 s_{12} \end{bmatrix} \tag{4.7} $$

$$ {}^{0}J = \begin{bmatrix} -L_1 s_1 - L_2 s_{12} & -L_2 s_{12} \\ L_1 c_1 + L_2 c_{12} & L_2 c_{12} \end{bmatrix} \tag{4.8} $$

To find the joint torques of the manipulator, the force at the end effector is multiplied by the transpose of the Jacobian matrix.

$$ \Gamma = \ {}^{0}\mathrm{J}^{\mathrm{T}} \ {}^{0}\mathrm{F}_{\mathrm{ee}} \tag{4.9} $$

The admittance control relation then uses these torques to calculate the desired joint angles for the next time step. The relation used is

$$\theta_j = k_{pa}\Gamma_e + k_{ia}\int \Gamma_e - k_{da}\,\dot{\theta}_j \tag{4.10}$$

where k_{pa}, k_{ia}, and k_{da} are the admittance control gains for the proportional, integral, and derivative terms, respectively [29]. The desired joint angles are then used as the set points in a PID control scheme. This is given by

$$v_{im}(t) = k_{pi}e_i(t) + k_{ii}\int_0^t e_i(\tau)d\tau - k_{di}\dot{v}_{im}(t) \tag{4.11}$$

where v_{im} is the voltage output sent to the motor for joint i, e_i is the error for joint i, and k_{pi}, k_{ii}, and k_{di} are the PID gains for the i^{th} joint. Note that in (4.11), the usual derivative term $k_{di}\frac{de_i(t)}{dt}$ is replaced with the gain k_{di} multiplied by the negative derivative of the voltage. This is done to prevent derivative kickback.

Figure 4.4 shows how the pieces developed above fit into the control strategy as a whole. First, the user of the exoskeleton exerts a force on the end effector. The force sensor, which is on the second link for the finger manipulators and the first link for the thumb manipulator, reads a component of that force in accordance with the angles of the links. It then outputs an analog voltage to the NI myRIO device. The signal goes through a low pass filter and is amplified and translated into a force. Using the previous equations, the force is transformed to the ground frame and the joint torques are calculated. These torques are used as the input to the admittance control block, and the new set point angles are calculated. A PID controller then outputs voltages to the motors to bring the manipulator to this desired position.

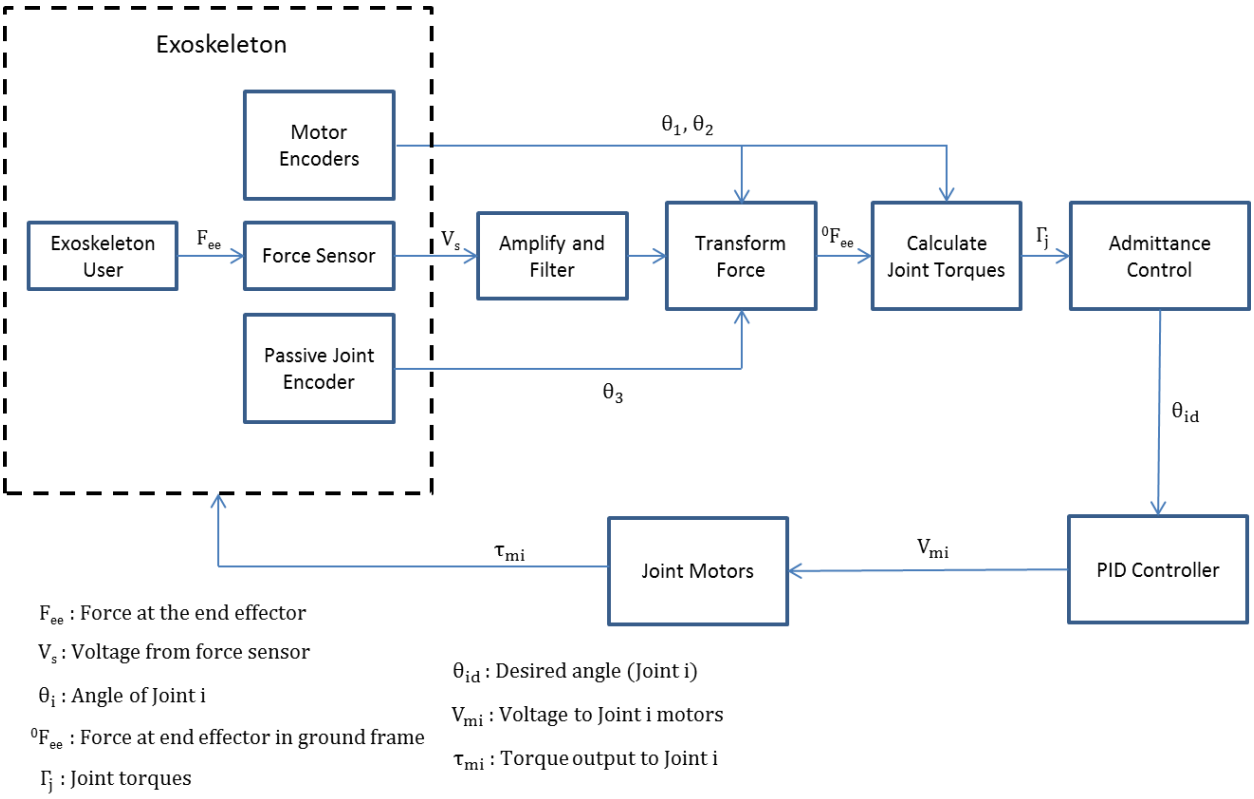

Figure 4.4: Diagram of Exoskeleton System and Control System Layout.

The scope of this thesis includes the initial determination of the gains for the admittance relation and PID controller. First, the gains for the PID controller were set. This was done in order to create the desired response of the motors/end effector/joints to changing angle set points. The qualitative objective was to create a response that resulted in movement that was subjectively comfortable to the human hand. Because steady state error is less of an issue in this system, a PD controller was used, and the integral gains for both joints were set to zero.

During testing, the proportional gain was increased until the system response began to oscillate. Following this, the derivative gains were increased from zero until the system settled within the desired time. It was observed during tuning that for a given set of gains, the system response varied in response to steps of various sizes, indicating nonlinearity in the system.

Therefore the PID gains were tuned using set point changes of approximately 10 degrees, which are still higher than those that the admittance control algorithm is expected to attempt.

The admittance relations were the next focus. These parameters influence the trajectory of the end effector that the controller plans at each time step in response to the force exerted at the end effector by the exoskeleton's user. For initial testing of the control algorithm, only the proportional gain was non-zero is used while the effects of the integral and derivative terms on the trajectory as experimented with in more detail. This makes the change in the motor's angles directly proportional to the force at the end effector, thereby control a straightforward "stiffness" in the manipulator. The values for both the admittance relation and PID controller gains used for initial testing are shown in Table 4.1.

Table 4.1: Parameters for the Admittance Relation and the PID Controller

Admittance Relation		**PID Controller**	
k_{pa}	0.750	k_p	0.100
k_{ia}	0	k_i	0
k_{da}	0	k_d	$1.75x10^{-3}$

4.2 Summary

In this chapter, the control system for the hand exoskeleton was presented. The system uses joint space admittance control and controls the relationship between the force input from the user to the end effector and the motion output. By using the tuning methods described, baseline gains for both the admittance and PID controllers were determined. These gains result in subjectively smooth motion for the wearer of the exoskeleton. These gains can be fine-tuned depending on the desired assistance and resistance from the exoskeleton while performing various grasps.

CHAPTER 5

Conclusion

This thesis has presented the mechanical design and base control algorithm of a dexterous hand exoskeleton for use in stroke patient rehabilitation. The exoskeleton controls the fingers and thumb with three 3R planar manipulators. The base positions of these manipulators can be adjusted, and the end effector interfaces with the user are designed to be switchable. Together, these give the exoskeleton the ability to manipulate different combinations of fingers and aid the user with a number of different types of grasps during rehabilitation exercises. A brute force kinematic optimization method was used as a tool to determine the manipulator link lengths, allowing the device to effectively accommodate a wide range of hand sizes. The exoskeleton's three manipulators are actuated by a remote motor pack through a system of capstans and Bowden cables. Each manipulator operates with an admittance control scheme and assists the user based on the input force to the end effector.

As the mechanical design for this exoskeleton is set, future work for this device focuses largely on the control system. This includes fine-tuning the gains for the admittance controller based on the overall control strategy. One factor to consider is how much assistance the user requires from the exoskeleton during certain motions or grasps. This opens up the possibility of a heuristic control system to learn which gain settings are appropriate and/or adjust these gains in real time.

Future work could also include the optimization algorithm. Adjustments can be made to the algorithm based on new data that might become available in the future. For instance, if the

relevant data becomes available, the algorithm—instead of optimizing manipulator kinematics for the entire desired workspace—could prioritize performance in sub-areas of the workspace that fingers are found to spend the most time in during activities of daily living, or those regions that stroke patients with spasticity have the most difficulty moving in. An optimization algorithm accounting for these data would aid in the mechanical design of any future iterations of the manipulators. Future iterations could also experiment with sensors of different types and smaller sizes. This could allow the force sensing to be done more proximally to the finger interface. Sensors from cell phone technology could also be incorporated into the main body of the exoskeleton hand itself to sense its absolute orientation relative to other components of the entire upper-limb exoskeleton.

Bibliography

[1] American Heart Associ, “AHA Statistical Update Heart Disease and Stroke Statistics — 2014 Update,” 2014.

[2] D. K. Sommerfeld, E. U. Eek, A. Svensson, L. W. Holmqvist, M. H. Von Arbin, and B. Index, “Spasticity After Stroke,” *Stroke*, vol. 35, no. 1, pp. 134–139, 2003.

[3] D. K. Sommerfeld, E. U. Eek, A. Svensson, L. W. Holmqvist, M. H. Von Arbin, and B. Index, “Spasticity After Stroke,” pp. 134–141, 2003.

[4] H. Visiting and H. Visiting, “Prevalence of spasticity post stroke,” pp. 515–522, 2002.

[5] J. H. Cauraugh and J. J. Summers, “Neural plasticity and bilateral movements : A rehabilitation approach for chronic stroke,” *Prog. Neurobiol.*, vol. 75, pp. 309–320, 2005.

[6] E. B. Brokaw, S. Member, I. Black, R. J. Holley, and P. S. Lum, “Hand Spring Operated Movement Enhancer (HandSOME): A Portable , Passive Hand Exoskeleton for Stroke Rehabilitation,” *IEEE Trans. NEURAL Syst. Rehabil. Eng.*, vol. 19, no. 4, pp. 391–399, 2011.

[7] C. N. Schabowsky, S. B. Godfrey, R. J. Holley, and P. S. Lum, “Development and pilot testing of HEXORR : Hand EXOskeleton Rehabilitation Robot,” *J. Neuroeng. Rehabil.*, vol. 7, no. 36, pp. 1–16, 2010.

[8] Y. Fu and S. Wang, “Development of a Multi-DOF Exoskeleton Based Machine for Injured Fingers,” in *IEEE/RSJ International Conference on Intelligent Robots and Systems*, 2008, pp. 22–26.

[9] T. T. Worsnopp, M. A. Peshkin, J. E. Colgate, and D. G. Kamper, “An Actuated Finger Exoskeleton for Hand Rehabilitation Following Stroke,” in *IEEE 10th International Conference on Rehabilitation Robotics*, 2007, pp. 1–6.

[10] C. L. Jones, S. Member, F. Wang, R. Morrison, S. Member, N. Sarkar, S. Member, and D. G. Kamper, “Design and Development of the Cable Actuated Finger Exoskeleton for Hand Rehabilitation Following Stroke,” *IEEE/ASME Trans. MECHATRONICS*, vol. 19, no. 1, pp. 131–140, 2014.

[11] P. Agarwal, J. Fox, Y. Yun, M. K. O. Malley, and A. D. Deshpande, “An index finger exoskeleton with series elastic actuation for rehabilitation : Design , control and performance characterization,” 2015.

[12] M. Cempini, M. Cortese, and N. Vitiello, “A powered finger-thumb wearable hand exoskeleton with self-aligning joint axes,” *IEEE/ASME Trans. Mechatronics*, vol. 20, no. 2, pp. 705–716, 2015.

[13] S. W. Lee, K. A. Landers, and H. Park, “Biomimetic Hand Exotendon Device (BiomHED) for Functional Hand Rehabilitation in Stroke,” in *IEEE International Conference on Rehabilitation Robotics*, 2013, pp. 13–16.

[14] A. Chiri, N. Vitiello, S. Member, F. Giovacchini, S. Roccella, F. Vecchi, M. C. Carrozza, and A. Member, “Mechatronic Design and Characterization of the Index Finger Module of a Hand Exoskeleton for Post-Stroke Rehabilitation,” *IEEE/ASME Trans. Mechatronics*, vol. 17, no. 5, pp. 884–894, 2012.

[15] Y. Yun, P. Agarwal, J. Fox, K. E. Madden, and A. D. Deshpande, “Accurate Torque Control of Finger Joints with UT Hand Exoskeleton through Bowden Cable SEA.”

[16] C. G. Rose, F. Sergi, Y. Yun, K. Madden, A. D. Deshpande, and M. K. O. Malley, “Characterization of a hand-wrist exoskeleton , READAPT , via kinematic analysis of redundant pointing tasks.”

[17] Y. Ren, H. Park, and L. Zhang, “Developing a whole-arm exoskeleton robot with hand

opening and closing mechanism for upper limb stroke rehabilitation," in *IEEE 11th International Conference on Rehabilitation Robotics*, 2009, pp. 761–765.

[18] P. Polygerinos, Z. Wang, K. C. Galloway, R. J. Wood, and C. J. Walsh, "Soft robotic glove for combined assistance and at-home rehabilitation," *Rob. Auton. Syst.*, vol. 73, pp. 135–143, 2015.

[19] B. H. Zhao, J. Jalving, R. Huang, R. Knepper, A. Ruina, and R. Shepherd, "A Helping Hand," no. September, pp. 55–64, 2016.

[20] Z. G. Xiao and C. Menon, "Towards the Development of a Portable Wrist Exoskeleton," pp. 1884–1889, 2011.

[21] Z. O. Khokhar, Z. G. Xiao, and C. Menon, "Surface EMG pattern recognition for real-time control of a wrist exoskeleton," pp. 1–17, 2010.

[22] I. A. Kapandji, *The Physiology of the Joints Upper Limb, Volume 1*, 5th ed. Churchville Livingstone, 1983.

[23] T. Greiner, "Hand Anthropometry of U.S. Army Personnel," 1991.

[24] M. R. Cutkosky, "On Grasp Choice, Grasp Models, and the Design of Hands for Manufacturing Tasks," *IEEE Trans. Robot. Autom.*, vol. 5, no. 3, pp. 269–279, 1989.

[25] A. Schiele, P. Letier, R. van der Linde, and F. van der Helm, "Bowden Cable Actuator for Force-Feedback Exoskeletons," in *International Conference on Intelligent Robots and Systems*, 2006, pp. 3599–3604.

[26] M. Sarac, M. Solazzi, E. Sotgiu, M. Bergamasco, and A. Frisoli, "Design and kinematic optimization of a novel underactuated robotic hand exoskeleton," *Meccanica*, vol. 51, pp. 1–13, 2016.

[27] J. Iqbal, N. Tsagarakis, and D. Caldwell, "Design Optimization of a Hand Exoskeleton

Rehabilitation Device," in *RSS workshop on understanding the human hand for advancing robotic manipulation*, 2009, pp. 1–2.

[28] J. Rosen, B. Hannaford, and R. Satava, Eds., *Surgical Robotics: Systems Applications and Visions*. Springer, 2010.

[29] L. M. Miller and J. Rosen, "Comparison of Multi-Sensor Admittance Control in Joint Space and Task Space for a Seven Degree of Freedom Upper Limb Exoskeleton."